Analysis, Design, and Implementation of a Differential Power Processing DMPPT With Multiple Buck–Boost Choppers for Photovoltaic Module

Jiahui Jiang, *Member, IEEE*, Tao Zhang, and Daolian Chen, *Senior Member, IEEE*

***Abstract*—Submodule mismatch has become the major cause of losses in the photovoltaic (PV) power generation system, which has been an important factor restricting the development of PV technology. Differential power processing (DPP) architecture is increasingly employed in PV distributed MPPT (DMPPT) due to its low processed power. In order to improve the PV utilization efficiency, minimize the power loss and reduce the system cost, a novel scheme based on DPP is introduced in this article. The proposed DPP converter is composed of multiple buck–boost choppers, and a multidimensional perturb and observe (MPO) algorithm is proposed to achieve true DMPPT through correcting the voltage of each submodule to its voltage at the maximum power point by using a single current sensor. A prototype with multiple buck–boost choppers for 36 V/200 W PV module is designed and built to verify the operating principle and evaluate the performance of the proposed DPP converter and DMPPT strategy, and the experimental results show that the prototype is low-cost and effectively improves system efficiency.**

***Index Terms*—Differential power processing (DPP), multidimensional perturb and observe, multiple buck–boost choppers, photovoltaic (PV) module, submodule distributed MPPT (DMPPT).**

I. Introduction

IN PHOTOVOLTAIC (PV) generation systems, PV elements (cells, submodules, and modules) often have mismatched *I–U* characteristics due to partial shading condition (PSC), manufacturing variability, and nonuniform aging, etc. Since the serial elements share the same current, some PV elements cannot operate at their individual maximum power point (MPP), and the output power of the system is limited by the underperforming elements [1]–[5]. By installing bypass diodes on each submodule, the mismatch can be mitigated and PV hot spotting can be prevented, but the power loss is still significant when a severe mismatch exists among submodules [6]–[8].

Manuscript received October 26, 2020; revised January 18, 2021; accepted February 25, 2021. Date of publication March 3, 2021; date of current version June 1, 2021. This work was supported by the Key Project of Natural Science Foundation of China, under Grant 51537001. Recommended for publication by Associate Editor J. Popovic-Gerber. *(Corresponding authors: Tao Zhang; Jiahui Jiang.)*

The authors are with the College of Electrical Engineering, Qingdao University, Qingdao 266071, China (e-mail: qdujiangjiahui@sina.com; zhangtao.2100@qq.com; chendaolian@hotmail.com).

Color versions of one or more figures in this article are available at https://doi.org/10.1109/TPEL.2021.3063230.

Digital Object Identifier 10.1109/TPEL.2021.3063230

In order to recover the power loss due to PV module or submodule mismatch, full power processing (FPP), and differential power processing (DPP) distributed MPPT (DMPPT) architectures, as shown in Fig. 1, are introduced. DC optimizer [9]–[12] and microinverter [13]–[15], as shown in Fig. 1(a) and (b), are two typical FPP architectures with a good performance, which are widely used in module-level DMPPT application. By installing a microinverter on the port of each PV element, it is easy to realize MPPT of each element, and only includes single-stage power conversion. However, the step-up ratio of the inverter is too high, which leads to the problem of high loss. Moreover, the cost of installing an inverter or a dc optimizer in each submodule is too high, so it is currently difficult to popularize the application at submodule level. In addition, FPP PV optimizers process full power of attached PV elements, leading to an inevitably inefficiency of the system.

By contrast, DPP architecture is a cost-effective power management solution for DMPPT application, as shown in Fig. 1(c)–(f). DPP architecture enjoys several advantages, such as higher efficiency, fewer components, and lower cost, since DPP converters process only a small portion of the power delivered by each PV element and is connected in a way that they process zero power in the absence of mismatch. Even if the conversion efficiency of DPP converters is lower than that of FPP converters, the overall system efficiency is still relatively high. Therefore, the DPP architecture can reduce the hardware size and cost of the power converter, which facilitates its integration with PV submodules and even smaller-grained PV elements. The submodule-level DPP are categorized into three types, which are different in connection: PV–PV [16]–[26], PV-bus [18], [27]–[34], and PV-isolated port bus (PV-IP) [27], [29], [35]–[37]. In PV–PV, the task of the converter is to realize the mismatch compensation current flow between adjacent submodules. The voltage stress of the power components in PV–PV is lower than that of the other two architectures. The architecture is scalable in the number of PV elements, but this work is not easy, because converters require all the PV elements to participate in power compensation, which introduce more power loss. In PV-bus, the mismatch compensation current flows between the PV submodules and dc bus. The advantage of the PV-bus architecture is that its processing power is reduced compared to the other two architectures. In PV-IP, the mismatch compensation current flows between the PV submodules and an isolated bus, and the voltage stress of power devices can be very small. Compared to FPP PV optimizers, the lower power rating of DPP converters

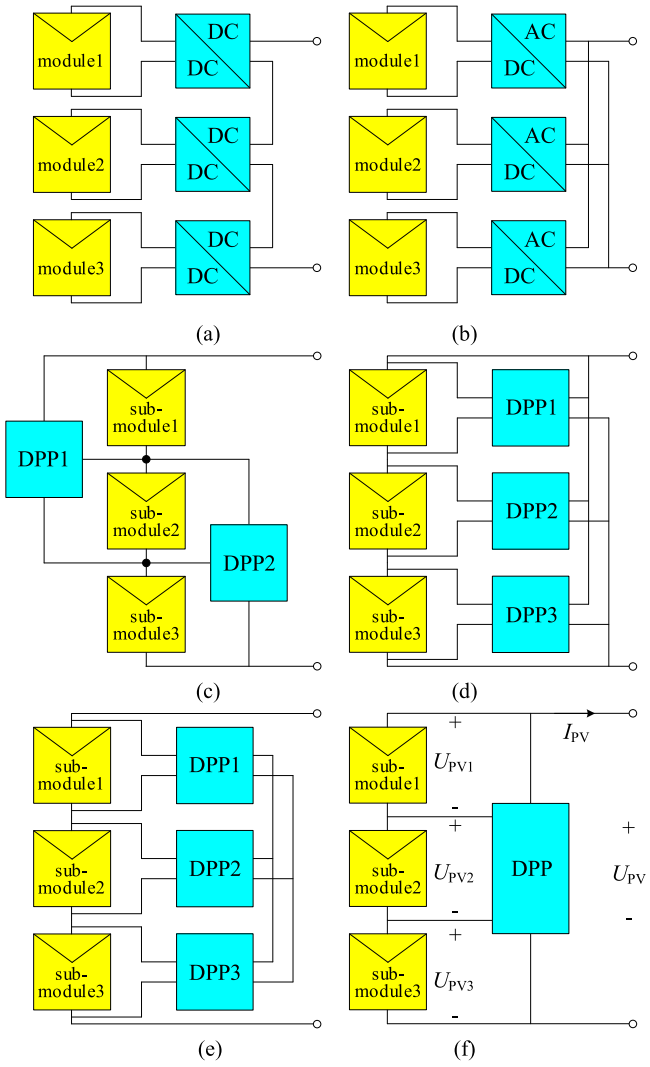

Fig. 1. PV DMPPT power generation systems. (a) DC optimizer. (b) Microinverter. (c) PV–PV DPP system. (d) PV-bus DPP system. (e) PV-IP DPP system. (f) More integrated DPP system.

offers potential cost reduction and reliability enhancement as well as higher efficiency in submodule level DMPPT.

In the research on DPP architecture, circuit topologies and control methods as the research focus had achieved excellent works. Many topologies, such as bidirectional buck–boost converter [16]–[22], switched capacitor converter [23], [24], resonant switched capacitor converter [25], [26], flyback converter [18], [27]–[33], [35], [36], Sepic converter [34], and power electronics equalizer [37], have been introduced. In the abovementioned topologies, the control method can be divided into two main types, including voltage equalization (VE) and true MPPT. Usually, VE can make the voltage of each PV element equal. This is based on a theory that the difference of voltage of mismatched PV elements is paltry. However, the characteristics of PV elements are often significantly different, and PV array installed outdoors can easily cause uneven aging, which makes VE unable to obtain valuable optimization results. But true MPPT control method could solve this problem since it is not affected by the difference in characteristics among PV elements. The DPP converter in [18] achieves true MPPT without using local distributed current sensors, which significantly reduces hardware costs and measurement loss, but requires additional communication modules. The literature [21] introduced the delta-conversion concept that aims at averaging out differences in output power between PV cells for PV submodules and modules, and it has made a contribution to reducing costs and expanding the scale of applications, but it brings difficulty to communication and has potential problems of low efficiency caused by multistage conversion. The circuit implementation of the switched-capacitor converters proposed in [23] for PV power management eliminates large power magnetic components, and a topology proposed in [24] reduces the voltage stress of the capacitor by half from the conventional switched-capacitor converter. A resonant switched-capacitor converter, which realized local MPPT is introduced in [26] by inserting an inductor in a switched-capacitor converter. The work in [28] proposed the concept of PV balancers and implemented two balancer structures, including flyback converter and flipped buck converter for isolated PV elements, but it requires a high-voltage transformation ratio at the inverter stage. The power electronics equalizer proposed in [37] employed only one magnetic component, but could not achieve true DMPPT, and used too many diodes. A detailed comparison of typical DPP topologies is presented in Table I. The number of switches, drivers, diodes, transformers, and auxiliary power supply of the proposed topology is reduced, which is conducive to further integration and cost reduction of the converter, and the overall performance of the converter is satisfactory.

The conventional DPP systems, as shown in Fig. 1(c)–(e), are often implemented as multiple bidirectional dc–dc converters. Either one converter connects two neighboring PV elements, or two converters connect two nonneighboring PV elements via an intermediate link. In short, the power is transferred inevitably with two-stage conversion among the PV elements. In order to reduce the power conversion loss and the number of current sensors, a more integrated DPP system is introduced in this article as shown in Fig. 1(f), and the objective of this article is to demonstrate a united and efficient submodule level DMPPT scheme with multiple buck–boost choppers to alleviate the energy loss that occurs due to mismatches in PV generation systems. Moreover, in the application of large-scale PV arrays, the scheme in this article is suitable for forming a matrix architecture with module-level DPP converters and module-level microinverters. The module-level DPP converters and the proposed DMPPT converters are independent, and the communication module is installed in the microinverter matrix. The specific implementation of this scheme is discussed in detail, and experimental verification is carried out.

The remainder of this article is organized as follows. Section II discusses the mismatch model of PV cells and submodules. Section III analyzes the DMPPT strategy based on the multidimensional perturb and observe algorithm. The topology, working principle, and control strategy are also proposed and studied. Section IV implements a prototype, and the experimental results are provided. Finally, Section V concludes this article.

II. PV Module and Mismatch

A. PV Model

A single-diode electrical equivalent circuit model is well known for circuit modeling for PV cells, as shown in Fig. 2.

TABLE I
COMPARISON OF DIFFERENT DPP TOPOLOGIES

Architecture	Topology	Semiconductor devices (switches+diodes)	Magnetic devices (transformers +inductors)	Auxiliary powers	Tracking method	Conversion efficiency
PV-PV	Buck-Boost[16]-[22]	4 (4+0)	2 (0+2)	2	TM*[17][19] VE[16][21]	89.0-95.0%
	Switched capacitor[23][24]	6 (6+0)	0	3	VE	84.0%
	Resonant switched capacitor[25][26]	6 (6+0)	2 (0+2)	3	TM[26] VE[25]	90.0%
PV-bus	PV-bus flyback[27]-[30]	6 (6+0)	3 (3+0)	3	TM[28][30] VE[27][29]	87.0-92.2%
	Multi-winding flyback[31]	7 (3+4)	1 (1+0)	4	TM	90.5%
	Boost-flyback[32][33]	8 (7+1)	4 (3+1)	3	TM[32] VE[33]	91.8-92.0%
	Sepic[34]	4 (1+3)	4 (0+4)	1	VE	90.0%
PV-IP	PV-IP flyback[35][36]	6 (6+0)	3 (3+0)	3	VE	Not reported
	Power electronics equalizer [37]	14 (6+8)	1 (0+1)	4	VE	Not reported
	Proposed topology	3 (3+0)	2 (0+2)	1	TM	92.3%**

*TM is short for true MPPT.
**Bases on the data obtained from experiment under closed-loop control, including digital circuit loss, sampling loss, driving loss, and auxiliary power loss (level conversion loss), etc. Detailed data and analysis are shown in Section IV.

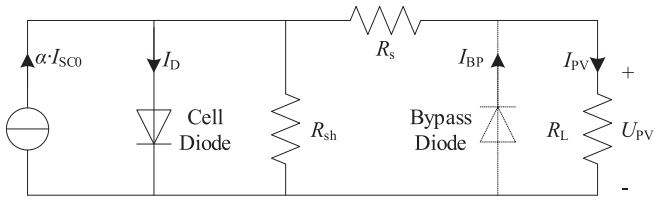

Fig. 2. Equivalent circuit model of a PV cell.

The *I–U* characteristic equation of a PV cell is given by the following equation:

$$I_{PV} = (\alpha I_{SC0} + C_t (T - T_{REF})) - I_{D0}\left(\exp\left(\frac{q(U_{PV} + R_s I_{PV})}{NAKT}\right) - 1\right) - \frac{U_{PV} + R_s I_{PV}}{R_{sh}} \quad (1)$$

where U_{PV} and I_{PV} are, respectively, the voltage and current of the series connected PV cells, α is the normalized irradiance ($0 \le \alpha \le 1$), I_{SC0} is the short-circuit current, I_{D0} is the saturation current, q is the electric charge of a single electron, A is the PV cell ideality factor, K is the Boltzmann constant, and N is the number of PV cells in series.

Ignoring the temperature change of the PV cells and the resistances R_{sh} and R_s in the model, (1) can be simplified as

$$I_{PV} = \alpha I_{SC0} - I_{D0}\left(\exp\left(\frac{qU_{PV}}{NAKT}\right) - 1\right). \quad (2)$$

Power–voltage equation of PV cells can be written as

$$P_{PV} = U_{PV}\left(\alpha I_{SC0} - I_{D0}\left(\exp\left(\frac{qU_{PV}}{NAKT}\right) - 1\right)\right). \quad (3)$$

When the bypass diodes are employed to solve the PV mismatch problem, the equivalent circuit model of PV cells can be expressed as

$$I_{PV} = \alpha I_{SC0} - I_{D0}\left(\exp\left(\frac{qU_{PV}}{AKT}\right) - 1\right) + I_{S0}\left(\exp\left(-\frac{qU_{PV}}{nKT}\right) - 1\right) \quad (4)$$

$$P_{PV} = U_{PV}\left(\alpha I_{SC0} - I_{D0}\left(\exp\left(\frac{qU_{PV}}{AKT}\right) - 1\right) + I_{S0}\left(\exp\left(-\frac{qU_{PV}}{nKT}\right) - 1\right)\right) \quad (5)$$

where I_{S0} and n are the saturation reverse current and idealized factor of the bypass diodes, respectively.

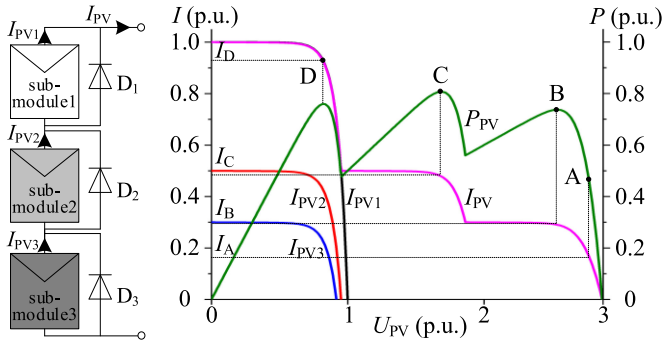

Fig. 3. Submodules with bypass diodes and the characteristic curves.

B. Mismatched PV Model

In commercial applications, an integrated PV panel (PV module) is often made up of three submodules. Therefore, the circuit topology and control strategy proposed in this article are dedicated to this type of PV panel, and so are the mathematical calculations. But it is worth noting that the proposed scheme can also be optimized and applied to PV panels containing a different number of submodules, such as two and four. Suppose that the irradiance of submodule 1, 2, and 3 subjects to $\alpha_1 > \alpha_2 > \alpha_3$, Fig. 3 shows PV submodules with bypass diodes and the output characteristic curves. It reveals that even if the bypass diode is employed, the power of the PV cells cannot be fully captured, which leads to a large power loss, and the *P–U* curve has multiple

peaks, which increases the complexity of MPPT. Based on the abovementioned theories, a novel multiple buck–boost choppers topology with a small volume and fewest sensors and DMPPT strategy are proposed in this article.

III. Implementation of Differential Power Processing DMPPT With Multiple Buck–Boost Choppers

In order to achieve the MPP and improve the utilization efficiency (MPPT efficiency) of the PV cells, the voltages (or currents) of the three submodules must be tracked to their own submodule MPP voltages (or currents), since the voltages and currents at the MPP of PV cells are various under different irradiance condition. The whole tracking process could be divided into module-level MPPT and submodule-level DMPPT. The module-level MPPT is used to achieve the tracking of the output voltage $U_{\rm PV}$, by the cascaded microinverter; the submodule-level DMPPT achieves the independent control of the three submodule voltages. Since the module-level MPPT operation frequency is usually much lower than the submodule-level DMPPT control frequency, these two control loops operate independently from each other simultaneously. The research in this article only focuses on the submodule-level DMPPT. By default, the module-level MPPT has finished the output voltage $U_{\rm PV}$ tracking.

The DPP DMPPT architecture with multiport choppers is shown in Fig. 1(f). By controlling multiple variables of the DPP converter, the voltage adjustment of three submodules is realized, thereby achieving true DMPPT of the PV module.

A. Analysis of DMPPT Characteristics of PV Module

Assume that the irradiances, submodule voltages, and submodule MPP voltages are α_i, $U_{{\rm PV}i}$, and $U_{{\rm PV}i{\rm m}}$ (i = 1, 2, 3), and $U_{\rm PV1}/U_{\rm PV} = a$, $U_{\rm PV2}/U_{\rm PV} = b$, and $U_{\rm PV3}/U_{\rm PV} = c$, where $a+b+c = 1$.

According to (3), the total output power of the PV module is

$$\begin{aligned} P_{\rm PV}(a,b) = {} & a\cdot U_{\rm PV}\left(\alpha_1 I_{\rm SC0} - I_{\rm D0}\left(\exp\left(\frac{a\cdot {\rm q}U_{\rm PV}}{{\rm NAK}T}\right)-1\right)\right) \\ & + b\cdot U_{\rm PV}\left(\alpha_2 I_{\rm SC0} - I_{\rm D0}\left(\exp\left(\frac{b\cdot {\rm q}U_{\rm PV}}{{\rm NAK}T}\right)-1\right)\right) \\ & + (1-a-b)\cdot U_{\rm PV}\left(\alpha_3 I_{\rm SC0} - I_{\rm D0}\right. \\ & \left.\times\left(\exp\left(\frac{(1-a-b)\cdot {\rm q}U_{\rm PV}}{{\rm NAK}T}\right)-1\right)\right). \end{aligned} \tag{6}$$

The first-order and second-order partial derivatives of $P_{\rm PV}(a, b)$ with respect to a are obtained as

$$\begin{aligned} \frac{\partial P_{\rm PV}(a,b)}{\partial {\rm a}} = {} & U_{\rm PV} I_{\rm D0}\left(\frac{I_{\rm SC0}}{I_{\rm D0}}(\alpha_1-\alpha_3) - \exp\left(\frac{a\cdot {\rm q}U_{\rm PV}}{{\rm NAK}T}\right)\right. \\ & \times\left(\frac{a\cdot {\rm q}U_{\rm PV}}{{\rm NAK}T}+1\right) \\ & + \exp\left(\frac{(1-a-b)\cdot {\rm q}U_{\rm PV}}{{\rm NAK}T}\right) \\ & \left.\times\left(\frac{(1-a-b)\cdot {\rm q}U_{\rm PV}}{{\rm NAK}T}+1\right)\right) \end{aligned} \tag{7}$$

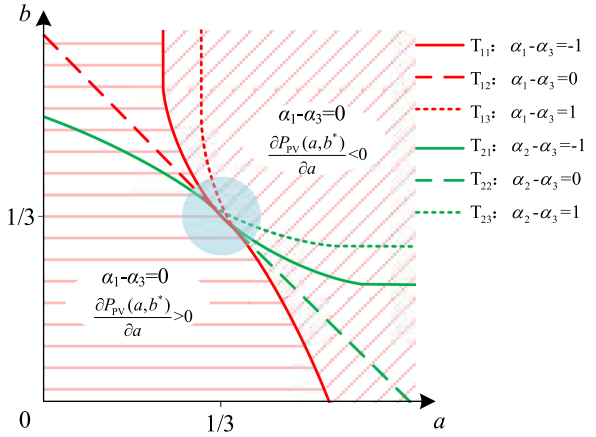

Fig. 4. Trajectory curves of the maximum point of function clusters $P_{\rm PV}$ (a, b^*) and $P_{\rm PV}$ (a^*, b).

$$\begin{aligned} \frac{\partial^2 P_{\rm PV}(a,b)}{\partial a^2} = {} & -U_{\rm PV} I_{\rm D0}\frac{{\rm q}U_{\rm PV}}{{\rm NAK}T}\left(\exp\left(\frac{a\cdot {\rm q}U_{\rm PV}}{{\rm NAK}T}\right)\right. \\ & \times\left(\frac{a\cdot {\rm q}U_{\rm PV}}{{\rm NAK}T}+2\right) \\ & + \exp\left(\frac{(1-a-b)\cdot {\rm q}U_{\rm PV}}{{\rm NAK}T}\right) \\ & \left.\times\left(\frac{(1-a-b)\cdot {\rm q}U_{\rm PV}}{{\rm NAK}T}+2\right)\right). \end{aligned} \tag{8}$$

Obviously, $\partial^2 P_{\rm PV}(a, b)/\partial a^2 < 0$. Hence, for $\forall b = b^* \in [0, 1]$, $\partial P_{\rm PV}(a, b^*)/\partial a$ decreases as a increases, and $P_{\rm PV}(a, b^*)$ has at most one maximal value point when $a \in [0, 1]$.

When $-1 \le \alpha_1 - \alpha_3 \le 1$, $-1 \le \alpha_2 - \alpha_3 \le 1$, the maximal point trajectory curves of function clusters $P_{\rm PV}(a, b^*)$ and $P_{\rm PV}(a^*, b)$ ($a^* \in [0, 1]$) are shown in Fig. 4. Where T_{11}, T_{12}, and T_{13} are the sets of maximum points of the function cluster $P_{\rm PV}(a, b^*)$ when α_1–$\alpha_3 = -1$, α_1–$\alpha_3 = 0$, and α_1–$\alpha_3 = 1$, respectively; T_{21}, T_{22}, and T_{23} are the sets of maximum points of the function cluster $P_{\rm PV}(a^*, b)$ when α_2–$\alpha_3 = -1$, α_2–$\alpha_3 = 0$, and α_2–$\alpha_3 = 1$, respectively. Under different irradiance conditions, for any $b = b^*$, in the area to the left of the trajectory T_{11} (or T_{12} or T_{13}), $P_{\rm PV}(a, b^*)$ increases with the increase of a, and in the area to the right of it, $P_{\rm PV}(a, b^*)$ decreases as a increases; similarly, for any $a = a^*$, in the area to the below of the trajectory T_{21} (or T_{22} or T_{23}), $P_{\rm PV}(a^*, b)$ increases as the increase of b, and in the area to the above of it, $P_{\rm PV}(a^*, b)$ decreases as the increase of b. The intersection point of the trajectories T_{1x} and T_{2y} ($x, y = 1, 2, 3$) is the MPP of the PV module under a certain voltage $U_{\rm PV}$ and irradiance condition. When $U_{\rm PV} = U_{\rm PV1m} + U_{\rm PV2m} + U_{\rm PV3m}$, the intersection point is exactly the distributed MPP (DMPP) of the PV module. Moreover, this DMPP exists in a domain centered on the point ($a = 1/3$, $b = 1/3$). Based on the abovementioned analysis, we can limit the operating point of the PV power generation system to a preset domain, which helps reduce the oscillation loss of MPPT, and it also plays a very important role in configuring the automatic reboot of the MPPT.

Therefore, the equation $U_{\rm PV} = U_{\rm PV1m} + U_{\rm PV2m} + U_{\rm PV3m}$ is true after the process of the module-level MPPT and the

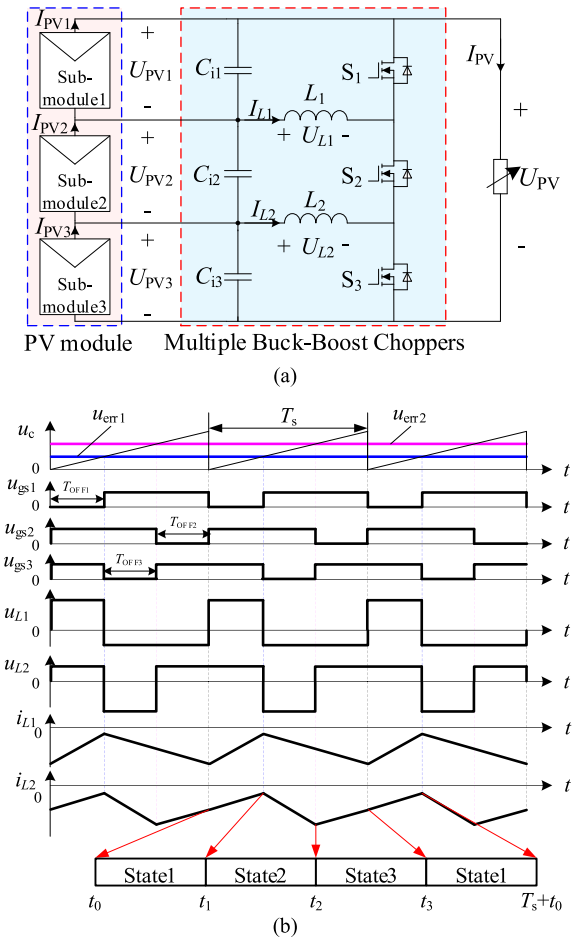

Fig. 5. Topology and waveforms. (a) Topology of DPP DMPPT with multiple buck–boost choppers topology. (b) Steady-state waveforms.

submodule-level DMPPT, and finally DMPPT is finished. In addition, the control of the submodule voltages can be equivalent to the control of the factors a, b, and c.

B. Topology and Working Principle of Multiport Buck–Boost Choppers

1) Topology of Multiport Buck–Boost Choppers: The introduced DPP DMPPT topology with multiport buck–boost choppers is shown in Fig. 5. The topology consists of two bidirectional buck–boost choppers. The switch S_1, the inductor L_1, and the switches $S_{2\text{and}3}$ constitute the bidirectional buck–boost chopper I; the switch S_3, the inductor L_2, and the switches $S_{1\text{and}2}$ constitute the bidirectional buck–boost chopper II. In these two choppers, the turn-ON time of S_1 is complementary to that of $S_{2\text{ and }3}$ with dead time, and so is S_3 and $S_{1\text{ and }2}$, and the direction and amplitude of the currents of L_1 and L_2 are controlled by adjusting the duty of S_1 and S_3, and then the three submodule voltages are controlled.

2) Working Principle of Multiple Buck–Boost Choppers: The direction and amplitude of the inductor currents, I_{L1} and I_{L2}, are various due to different irradiance of three submodules, and the relationship between the current directions and the irradiance is shown in the following equations:

$$I_{L1}\begin{cases} <0, & 2\alpha_1-\alpha_2-\alpha_3>0 \\ >0, & 2\alpha_1-\alpha_2-\alpha_3<0 \end{cases} \tag{9}$$

$$I_{L2}\begin{cases} <0, & \alpha_1+\alpha_2-2\alpha_3>0 \\ >0, & \alpha_1+\alpha_2-2\alpha_3<0. \end{cases} \tag{10}$$

Taking $\alpha_1>\alpha_2>\alpha_3$ as an example, $I_{L1}<0$, and $I_{L2}<0$. The working principle of this circuit is discussed as follows. The converter has three operating modes within one switch period according to the different states of S_1, S_2, and S_3, as shown in Fig. 6. $u_{\text{gs1–3}}$, u_{L1-2}, and i_{L1-2} are the drive signals of the three switches, the inductor voltages, and currents, respectively.

State 1: During $[t_0$–$t_1]$, S_2 and S_3 are reversely turned ON, and S_1 is turned OFF. As shown in Fig. 6(a), L_1 and L_2 are charged by U_{PV2} and U_{PV3} through S_2 and S_3.

State 2: During $[t_1$–$t_2]$, S_1 and S_2 are forward turned ON, and S_3 is turned OFF. As shown in Fig. 6(b), L_1 and L_2 are discharged by U_{PV1} and U_{PV2} through S_1 and S_2.

State 3: During $[t_2$–$t_3]$, S_1 is forward turned ON, S_3 is reversely turned ON, and S_2 is turned OFF. As shown in Fig. 6(c), L_1 is charged by U_{PV1} through S_1, and L_2 is discharged by U_{PV3} through S_3.

According to the volt–second balance of L_1 and L_2

$$(U_{\text{PV2}}+U_{\text{PV3}})\times T_{\text{OFF1}}-U_{\text{PV1}}\times(T_{\text{OFF2}}+T_{\text{OFF3}})=0 \tag{11}$$

$$(U_{\text{PV1}}+U_{\text{PV2}})\times T_{\text{OFF3}}-U_{\text{PV3}}\times(T_{\text{OFF1}}+T_{\text{OFF2}})=0. \tag{12}$$

Define the OFF duty of the switches

$$\overline{D}=T_{\text{OFF}}/T_{\text{S}} \tag{13}$$

where T_{S} and T_{OFF} are, respectively, the switching period and the OFF time of a switch within one switching period. The OFF duty of the switches S_1, S_2, and S_3 are $\overline{D_1}$, $\overline{D_2}$, and $\overline{D_3}$, respectively. Since S_1 and $S_{2\&3}$, S_3 and $S_{1\&2}$ work in complementarily

$$\overline{D_1}+\overline{D_2}+\overline{D_3}=1. \tag{14}$$

According to $U_{\text{PV1}}/U_{\text{PV}}=a$, $U_{\text{PV2}}/U_{\text{PV}}=b$, $U_{\text{PV3}}/U_{\text{PV}}=c$, and (11)–(14), (15) is true

$$\begin{cases} \overline{D_1}=a \\ \overline{D_2}=b \\ \overline{D_3}=c. \end{cases} \tag{15}$$

Therefore, the submodule voltages can be controlled by the OFF duty of S_1–S_3, and then achieve DMPPT of the PV module.

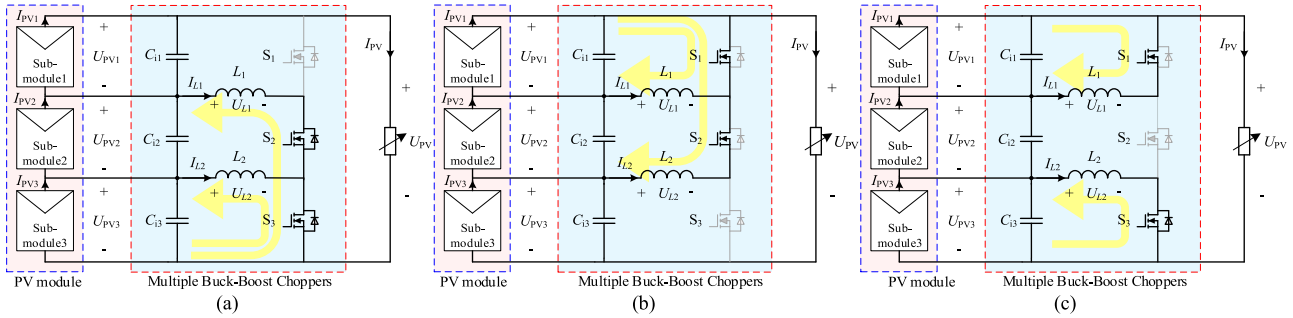

Fig. 6. Equivalent circuit of all states. (a) Equivalent circuit of state 1. (b) Equivalent circuit of state 2. (c) Equivalent circuit of state 3.

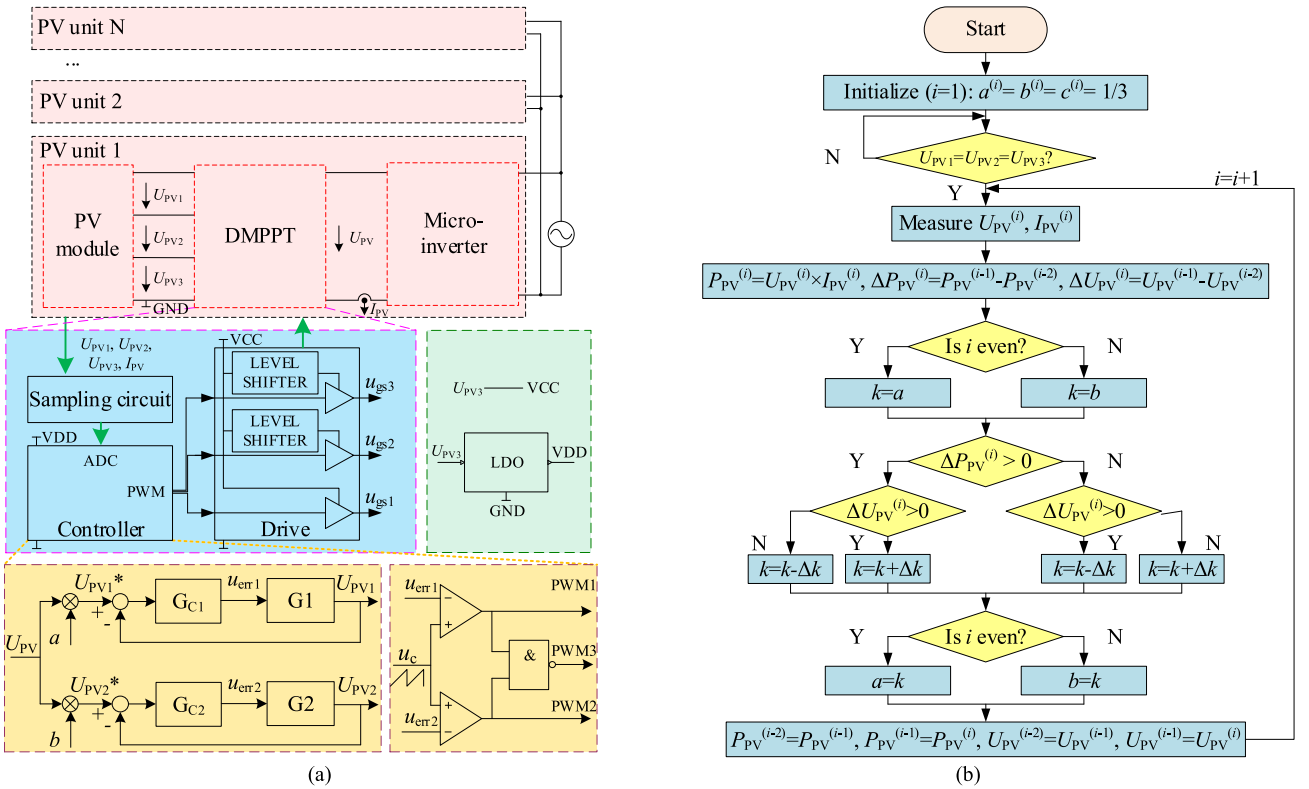

Fig. 7. Control system block diagram and flow chart. (a) Block diagram of the control system. (b) Iterative control flow chart of constant pressure equalization combined with multidimensional perturb and observe.

C. Design and Implementation of DMPPT Control System

The schematic of the proposed DMPPT system and the PV array generation system is shown in Fig. 7. The DMPPT control system consists of five parts, including main power circuit, control circuit, sampling circuit, drive circuit, auxiliary power supply, etc. These parts are all connected in a common ground (GND), with U_{PV3} as an auxiliary power supply. A small sensor resistor and resistor dividers are used to sample current and voltage, respectively. The driver comprises of two bootstrap circuits.

The system controls U_{PV3} indirectly by controlling U_{PV1} and U_{PV2}, and tracks the maximum power by sampling the voltage U_{PV} and current I_{PV} of the PV module. As mentioned in Section III, in this case, the proposed DPP converter and microinverter work together to achieve real-time tracking of three-dimensional vectors with main constraints and maximize the module current I_{PV} through the multidimensional perturb and observation (MPO) algorithm that perturbs the OFF duties and observes the increment of P_{PV} as illustrated by Fig. 7(b). When the submodule DMPPT process is launched, VE is started first to achieve fast tracking of approximate DMPP, which improves the response speed of the system; then MPO is started to achieve three-dimensional tracking of DMPP.

Fig. 8 presents the complete DMPPT process under $\alpha_1 = \alpha_3 = 1$, and $\alpha_2 = 0.1$. Before the DMPPT process is launched, the PV module achieves global MPP (point A) in multipeak P–U characteristics by module-level MPPT controller. The VE would be completed within the first few switching cycles of power-ON, and the operating point moves from A to B; then MPO optimizes the output power, and accurately tracks the operating point to point C, which is the DMPP point.

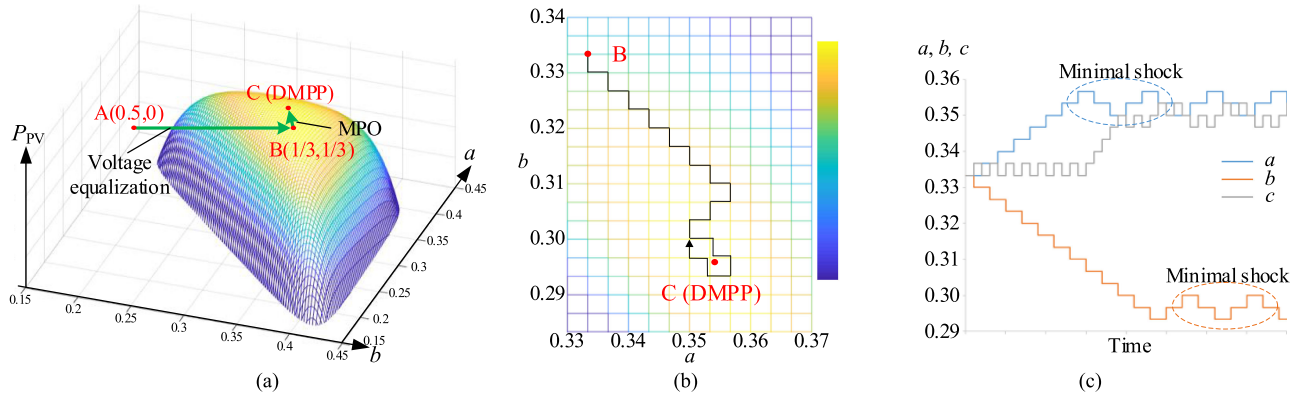

Fig. 8. Complete DMPPT process. (a) Complete DMPPT path. (b) MPO path. (c) MPO dynamic changes of a, b, c.

TABLE II
MAIN COMPONENT LIST

Device	Model/Value	Manufacturer	Unit Price ($)
Controller	STM32F030F4P6	ST	0.499
Amplifier	LM324PT	TI	0.104
MOSFET	CSD18543Q3A	TI	0.369
MOSFET	CSD88537ND	TI	0.513
Driver	LM5109BMAX	TI	0.527
Inductor	47μH	BOURNS	0.512

The prices of the device are from https://www.digikey.cn.

TABLE III
INSTRUMENTS AND MAIN PARAMETERS OF EXPERIMENT SETUP

Instruments	Model	Parameters	Value
Programmable power supply	Chroma 62020H-150S	Sub-module voltage at MPP	11.85V
Oscilloscopes	Keysight DSOX3034T	Sub-module current at MPP	5.626A

Fig. 8(b)–(c) presents the optimization paths of the voltage factors a, b, and c in MPO algorithm. Factors a and b are perturbed interleaved and the output power is observed. When both a and b enter the minimum pulsation mode, the DMPPT is finished. Note that the algorithm shown in the figure uses a fixed perturbation step size, but the variable step perturbation algorithm can be used to further improve the system's response speed and reduce the oscillation loss.

IV. EXPERIMENTAL RESULTS

A DPP DMPPT with multiple buck–boost choppers for 36 V/200 W PV module is designed and built to verify the operating principle and evaluate the performance of the proposed DPP converter and DMPPT strategy. The main component list of the experimental prototype and instruments and main parameters of experiment setup are shown in Tables II and III, respectively.

The DPP converter is implemented as a bidirectional synchronous buck–boost converter. Due to the small size of the converter, if it is combined with a centralized MPPT controller, it will consume little extra circuit board space; if it is implemented as an independent circuit, it is easy to be directly combined and installed in the PV module junction box. Moreover, the DPP converter itself has a simple structure, so it will not add greater complexity to the entire system.

A. Experimental Results

The photographs of the prototype are shown in Fig. 9, and Fig. 10 shows the experimental steady-state and dynamic results in a closed-loop manner to investigate its performance.

In the steady-state experiment, the irradiance is set to (α_1, α_2, α_3) = (1, 0.2, 1). Fig. 10(a) and (d) shows the driver voltage and submodule voltage waveform. Reverse-conducting switches (such as S_2) can be replaced with MOSFET body diodes, which reduces the control difficulty, but at the same time may cause additional power loss. Since the irradiance of submodule 2 is the lowest, its voltage is also the lowest, which is only 10.90 V, while that of the other two submodules is 11.85 V. In Fig. 10(b) and (e), before the sudden change in irradiance, the system has reached steady state, $U_{PV1} = U_{PV2} = U_{PV3} = 11.85$ V, $I_{PV1} = I_{PV2} = I_{PV3} = 5.63$ A, and all PV submodules work stably at their respective MPPs; after a sudden change in irradiance, the irradiance of submodule two decreases, so its MPP moves to the direction of decreasing voltage, U_{PV2} decreases to 11.69 V, whereas U_{PV1} and U_{PV3} increase to 11.93 V (since the total output voltage is the same as before the irradiance changes), correspondingly, I_{PV2} is rapidly reduced to 3.32 A, and I_{PV1} and I_{PV3} are reduced to 5.58 A at the same time. In Fig. 10(c) and (f), before the sudden change in irradiance, the irradiance of submodule 2 is lower than that of submodules 1 and 3, and its operating point voltage is also lower than that of submodules 1 and 3, $U_{PV1} = U_{PV3} = 11.93$ V, $U_{PV2} = 11.69$ V, $I_{PV1} = I_{PV3} = 5.58$ A, $I_{PV2} = 3.32$ A; after a sudden change in irradiance, the irradiance of submodule 2 rises to equal to that of submodules 1 and 3, and its MPP moves in the direction of voltage rise, U_{PV2} rises to 11.85 V, and U_{PV1} and U_{PV3} reduce to 11.85 V, the voltage of all submodules reach the same, correspondingly, I_{PV1}, I_{PV2}, and I_{PV3} are increased to 5.62 A at the same time, so the submodules work at the MPPs. The dynamic process lasted about 10 ms, after which the system reached a steady state again.

The experimental results show that the system output is stable, and the system can response to the irradiance change quickly, and the designed closed-loop control system can achieve superior control performance. The correctness of theoretical parameters and closed-loop design is proved.

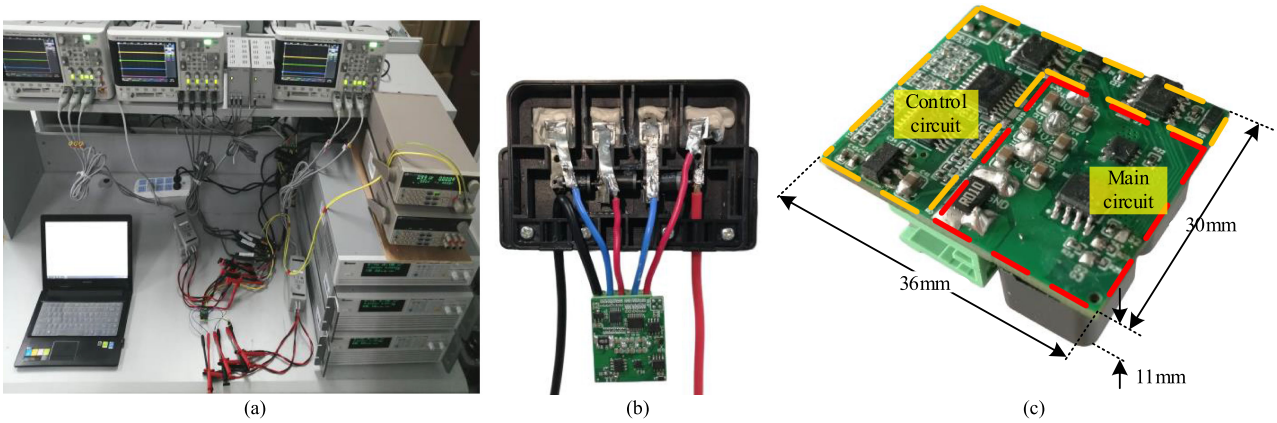

Fig. 9. Prototype photographs. (a) Indoor experiments setup. (b) Installed in PV panel junction box. (c) In detail.

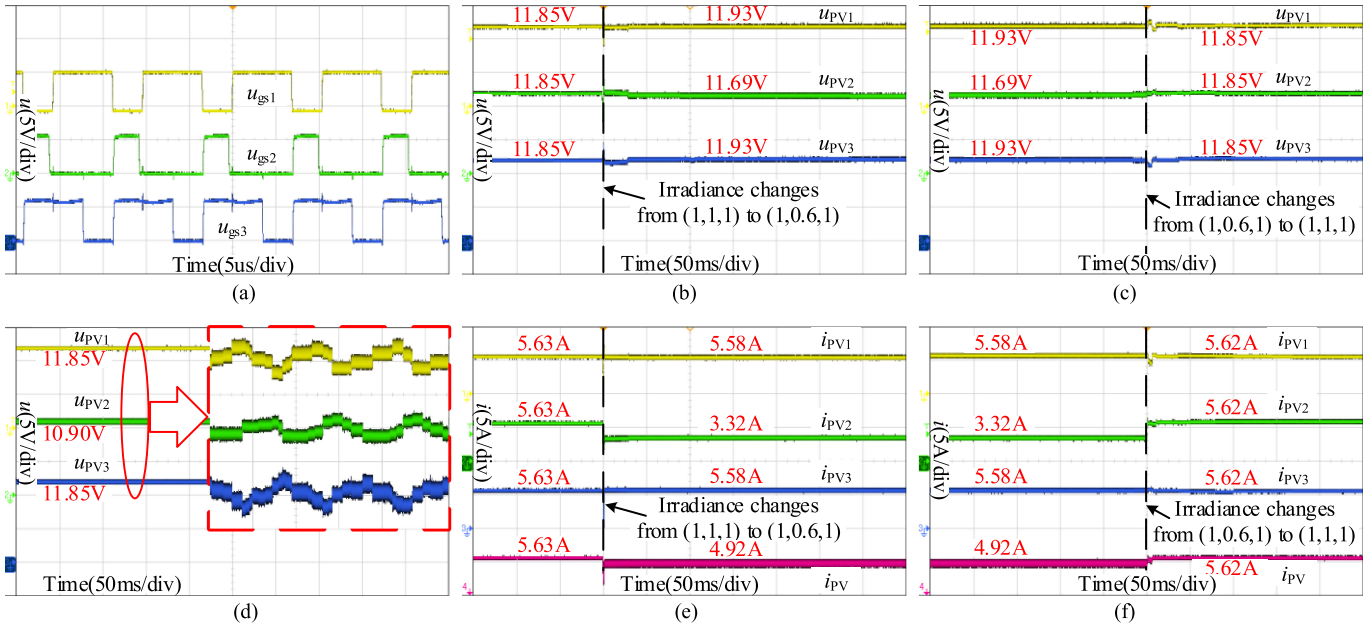

Fig. 10. Experimental waveforms. (a) Gate driver waveforms and (d) voltage waveforms when irradiance is ($\alpha 1$, $\alpha 2$, $\alpha 3$) = (1,0.2,1). (b) Voltage waveforms and (e) current waveforms when irradiance changes from (1,1,1) to (1,0.6,1). (c) Voltage waveforms and (f) current waveforms when irradiance changes from (1,0.6,1) to (1,1,1).

B. DC-Side Efficiency, Conversion Efficiency, and Utilization Efficiency

Considering various DPP architectures as described in Section I, how to evaluate the efficiency of a DPP system is a great challenge. It is obviously inappropriate to represent the efficiency of the whole system only by the conversion efficiency of one converter unit in the system. Therefore, this article proposes a method, that is, to regard the PV side and the load side as the input and output of the multiport bidirectional converter in a DPP system, and the dc-side efficiency in this article is defined as

$$\eta_{\rm dc}=\frac{P_{\rm load}}{P_{\rm PV}} \tag{16}$$

where $P_{\rm PV}$ and $P_{\rm load}$ are the output power of the PV module and the power of dc load or input power of cascaded centralized inverter, respectively.

Through this method, we can relatively fairly evaluate the efficiency of various topologies in different DPP architectures. This method is not affected by the number of input ports and output ports of a system, and can better compare the performance of different DPP architectures. In the experimental setup of this article, because the proposed converter includes multiple bidirectional ports, it is difficult to measure its actual conversion efficiency, but its dc-side efficiency is easy to get. The following is an analysis of the relationship between dc-side efficiency of the DPP system and equivalent conversion efficiency the converter. Its equivalent conversion efficiency can be written as

$$\eta_{\rm con}=1-\frac{P_{\rm PV}-P_{\rm load}}{P_{\rm process}} \tag{17}$$

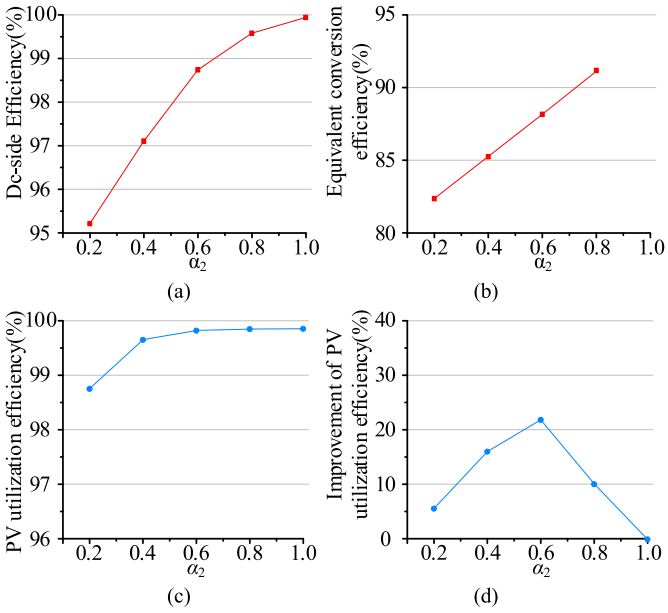

Fig. 11. Efficiency curves of $\alpha_1{=}\alpha_3{=}1$, $\alpha_2{=}0.2{\rightarrow}1$. (a) DC-side efficiency. (b) Equivalent conversion efficiency. (c) PV utilization efficiency. (d) Improvement of PV utilization efficiency compared to conventional scheme.

where P_{process} is the processed differential power of the DPP converter, and in the experimental setup of this article, P_{process} could be calculated as

$$P_{\text{process}}{=}\frac{|\alpha_1-\bar{\alpha}|+|\alpha_2-\bar{\alpha}|+|\alpha_3-\bar{\alpha}|}{2}\times\frac{200}{3}(\text{W}) \quad (18)$$

where $\bar{\alpha}=(\alpha_1{+}\alpha_2{+}\alpha_3)/3$.

The measured dc-side efficiency of the prototype, equivalent conversion efficiency of the converter, measured PV utilization efficiency, and improvement of PV utilization efficiency compared to conventional scheme are depicted in Fig. 11, and the dc-side efficiency is measured under closed-loop control, including digital circuit loss, sampling loss, driving loss, and auxiliary power loss (level conversion loss), etc., which can better reflect the characteristics of the system under actual working conditions. Fig. 11 shows the following.

1) The dc-side efficiency decreases with the increase in the severity of the PV submodule mismatch. When the irradiance is uniform ($\alpha_1 = \alpha_2 = \alpha_3 = 1$), the converter efficiency reaches nearly 100%, because all the generated power is transferred without being processed. As α_2 decreases, the efficiency also decreases. When $\alpha_2 = 0.2$, the converter efficiency decreases to 95.25%. This is mainly because of the higher power processed by the converter under severe mismatch conditions, and the conversion loss is also higher.
2) The equivalent conversion efficiency reaches 92.3% under slight mismatch conditions and over 80% under severe mismatch conditions.
3) According to the measured data, under closed-loop operating conditions, the PV utilization efficiency of the proposed converter under uniform irradiance condition ($\alpha_1 = \alpha_2 = \alpha_3 = 1$) is 99.81%; when the mismatch is not severer than $\alpha_1 = \alpha_3 = 1$ and $\alpha_2 = 0.4$, the PV utilization efficiency is higher than 99.65%. This means that the proposed converter works well with different inputs.
4) Compared with the conventional scheme of bypass diodes, the proposed scheme has a significant effect on the improvement of PV cell utilization efficiency, and the improvement reaches 21.19% when $\alpha_2 = 0.6$.

Hence, the proposed converter minimizes the number of components, and only employs an auxiliary power and drives three switches with the help of level shifters. Moreover, the converter realizes local true MPPT and compared with other references, the conversion efficiency is satisfactory.

V. Conclusion

This article discusses the development status of PV optimizers based on FPP and DPP architectures, and proposes a scheme with multiple buck–boost choppers based on DPP and an interleaved iterative MPO algorithm to achieve DMPPT and maximize the output power of PV module under PSC. In the proposed scheme, power is directly transmitted between submodules without any intermediary. The MPO algorithm is developed based on the DMPPT model of PV series mismatch, which can improve the dynamic response performance, reduce the oscillation loss, and realize true local MPPT. A prototype with a conversion efficiency of 92.3% for 200 W PV module is implemented. Experimental results show that the proposed algorithm can effectively track the local MPP, and the PV utilization efficiency is higher than 99.65% when the mismatch is not severe. This work has made contributions to miniaturization, cost reduction, and complexity reduction of the DPP converter, and provides a good reference for the further integration of hardware and PV submodule level DMPPT engineering applications, and provides experience for the future implementation of DMPPT at a higher level of granularity such as PV cell level.

References

[1] M. Adly and K. Strunz, "Efficient digital control for MPP tracking and output voltage regulation of partially shaded PV modules in DC bus and DC microgrid systems," *IEEE Trans. Power Electron.*, vol. 34, no. 7, pp. 6309–6319, Jul. 2019.
[2] E. Koutroulis, N. Sason, and V. Georgiadis, "Combined tracking of the maximum power and maximum efficiency operating points for real-time maximization of the energy production of PV systems," *IEEE Trans. Power Electron.*, vol. 34, no. 9, pp. 8634–8645, Sep. 2019.
[3] F. Rong, X. Gong, and S. Huang, "A novel grid-connected PV system based on MMC to get the maximum power under partial shading conditions," *IEEE Trans. Power Electron.*, vol. 32, no. 6, pp. 4320–4333, Jun. 2017.
[4] A. Kumaresan, H. Dehghani Tafti, K. Nandha Kumar, G. G. Farivar, J. Pou, and T. Subbaiyan, "Flexible power point tracking for solar photovoltaic systems using secant method," *IEEE Trans. Power Electron*, 2021, to be published, doi: 10.1109/TPEL.2021.3049275.
[5] P. Shukl and B. Singh, "Delta-Bar-Delta neural-network-based control approach for power quality improvement of solar-pv-interfaced distribution system," *IEEE Trans. Ind. Informat.*, vol. 16, no. 2, pp. 790–801, Feb. 2020.
[6] X. Li, H. Wen, Y. Hu, Y. Du, and Y. Yang, "A comparative study on photovoltaic MPPT algorithms under EN50530 dynamic test procedure," *IEEE Trans. Power Electron.*, vol. 36, no. 4, pp. 4153–4168, Apr. 2021.
[7] M. A. Ghasemi, H. M. Foroushani, and M. Parniani, "Partial shading detection and smooth maximum power point tracking of PV arrays under PSC," *IEEE Trans. Power Electron.*, vol. 31, no. 9, pp. 6281–6292, Sep. 2016.
[8] H. Li, D. Yang, W. Su, J. Lü, and X. Yu, "An overall distribution particle swarm optimization MPPT algorithm for photovoltaic system under partial shading," *IEEE Trans. Ind. Electron.*, vol. 66, no. 1, pp. 265–275, Jan. 2019.

[9] R. C. N. Pilawa-Podgurski and D. J. Perreault, "Submodule integrated distributed maximum power point tracking for solar photovoltaic applications," *IEEE Trans. Power Electron.*, vol. 28, no. 6, pp. 2957–2967, Jun. 2013.
[10] S. Sajadian and R. Ahmadi, "Distributed maximum power point tracking using model predictive control for photovoltaic energy harvesting architectures based on cascaded power optimizers," *IEEE J. Photovolt.*, vol. 7, no. 3, pp. 849–857, May 2017.
[11] C. Chen, K. Chen, and Y. Chen, "Modeling and controller design of an autonomous PV module for DMPPT PV systems," *IEEE Trans. Power Electron.*, vol. 29, no. 9, pp. 4723–4732, Sep. 2014.
[12] Y. Zhuang *et al.*, "A multiport modular DC-DC converter with low-loss series LC power balancing unit for MVDC interface of distributed photovoltaics," *IEEE Trans. Power Electron.*, vol. 36, no. 7, pp. 7736–7749, Jul. 2021.
[13] S. Harb and R. S. Balog, "Reliability of candidate photovoltaic module-integrated-inverter (PV-MII) Topologies—A usage model approach," *IEEE Trans. Power Electron.*, vol. 28, no. 6, pp. 3019–3027, Jun. 2013.
[14] M. A. Rezaei, K. Lee, and A. Q. Huang, "A high-efficiency flyback Micro-inverter with a new adaptive snubber for photovoltaic applications," *IEEE Trans. Power Electron.*, vol. 31, no. 1, pp. 318–327, Jan. 2016.
[15] W. Liang, Y. Liu, and J. Peng, "A day and night operational Quasi-Z source multilevel grid-tied PV power system to achieve active and reactive power control," *IEEE Trans. Power Electron.*, vol. 36, no. 1, pp. 474–492, Jan. 2021.
[16] S. Qin, C. B. Barth, and R. C. N. Pilawa-Podgurski, "Enhancing microinverter energy capture with submodule differential power processing," *IEEE Trans. Power Electron.*, vol. 31, no. 5, pp. 3575–3585, May 2016.
[17] P. S. Shenoy, K. A. Kim, B. B. Johnson, and P. T. Krein, "Differential power processing for increased energy production and reliability of photovoltaic systems," *IEEE Trans. Power Electron.*, vol. 28, no. 6, pp. 2968–2979, Jun. 2013.
[18] K. A. Kim, P. S. Shenoy, and P. T. Krein, "Converter rating analysis for photovoltaic differential power processing systems," *IEEE Trans. Power Electron.*, vol. 30, no. 4, pp. 1987–1997, Apr. 2015.
[19] S. Qin, S. T. Cady, A. D. Domínguez-García, and R. C. N. Pilawa-Podgurski, "A distributed approach to maximum power point tracking for photovoltaic submodule differential power processing," *IEEE Trans. Power Electron.*, vol. 30, no. 4, pp. 2024–2040, Apr. 2015.
[20] T. Shimizu, M. Hirakata, T. Kamezawa, and H. Watanabe, "Generation control circuit for photovoltaic modules," *IEEE Trans. Power Electron.*, vol. 16, no. 3, pp. 293–300, May 2001.
[21] H. J. Bergveld *et al.*, "Module-Level DC/DC conversion for photovoltaic systems: The delta-conversion concept," *IEEE Trans. Power Electron.*, vol. 28, no. 4, pp. 2005–2013, Apr. 2013.
[22] F. Wang, T. Zhu, F. Zhuo, and H. Yi, "An improved submodule differential power processing-based PV system with flexible Multi-MPPT control," *IEEE J. Emerg. Sel. Topics Power Electron.*, vol. 6, no. 1, pp. 94–102, Mar. 2018.
[23] J. T. Stauth, M. D. Seeman, and K. Kesarwani, "Resonant switched-capacitor converters for Sub-module distributed photovoltaic power management," *IEEE Trans. Power Electron.*, vol. 28, no. 3, pp. 1189–1198, Mar. 2013.
[24] M. Uno, M. Yamamoto, H. Sato, and S. Oyama, "Modularized differential power processing architecture based on switched capacitor converter to virtually unify mismatched photovoltaic panel characteristics," *IEEE Trans. Power Electron.*, vol. 35, no. 2, pp. 1563–1575, Feb. 2020.
[25] J. T. Stauth, M. D. Seeman, and K. Kesarwani, "A resonant switched-capacitor IC and embedded system for sub-module photovoltaic power management," *IEEE J. Solid-State Circuits*, vol. 47, no. 12, pp. 3043–3054, Dec. 2012.
[26] A. Blumenfeld, A. Cervera, and M. M. Peretz, "Enhanced differential power processor for PV systems: Resonant switched-capacitor gyrator converter with local MPPT," *IEEE J. Emerg. Sel. Topics Power Electron.*, vol. 2, no. 4, pp. 883–892, Dec. 2014.
[27] Y. Levron, D. R. Clement, B. Choi, C. Olalla, and D. Maksimovic, "Control of submodule integrated converters in the isolated-port differential power-processing photovoltaic architecture," *IEEE J. Emerg. Sel. Topics Power Electron.*, vol. 2, no. 4, pp. 821–832, Dec. 2014.
[28] H. Zhou, J. Zhao, and Y. Han, "PV balancers: Concept, architectures, and realization," *IEEE Trans. Power Electron.*, vol. 30, no. 7, pp. 3479–3487, Jul. 2015.
[29] C. Olalla, D. Clement, M. Rodriguez, and D. Maksimovic, "Architectures and control of submodule integrated DC–DC converters for photovoltaic applications," *IEEE Trans. Power Electron.*, vol. 28, no. 6, pp. 2980–2997, Jun. 2013.
[30] G. Chu, H. Wen, Y. Yang, and Y. Wang, "Elimination of photovoltaic mismatching with improved submodule differential power processing," *IEEE Trans. Ind. Electron.*, vol. 67, no. 4, pp. 2822–2833, Apr. 2020.
[31] H. Delavaripour, B. M. Dehkordi, H. A. Zarchi, and E. Adib, "Increasing energy capture from partially shaded PV string using differential power processing," *IEEE Trans. Ind. Electron.*, vol. 66, no. 10, pp. 7672–7682, Oct. 2019.
[32] Y. Jeon and J. Park, "Unit-Minimum least power point tracking for the optimization of photovoltaic differential power processing systems," *IEEE Trans. Power Electron.*, vol. 34, no. 1, pp. 311–324, Jan. 2019.
[33] G. Chu, H. Wen, Y. Hu, L. Jiang, Y. Yang, and Y. Wang, "Low-Complexity power balancing point-based optimization for photovoltaic differential power processing," *IEEE Trans. Power Electron.*, vol. 35, no. 10, pp. 10306–10322, Oct. 2020.
[34] M. Uno and A. Kukita, "Current sensorless equalization strategy for a single-switch voltage equalizer using multistacked buck–boost converters for photovoltaic modules under partial shading," *IEEE Trans. Ind. Appl.*, vol. 53, no. 1, pp. 420–429, Jan./Feb. 2017.
[35] G. Chu, H. Wen, L. Jiang, Y. Hu, and X. Li, "Bidirectional flyback based isolated-port submodule differential power processing optimizer for photovoltaic applications," *Sol. Energy*, vol. 158, pp. 929–940, Nov. 2017.
[36] C. Olalla, C. Deline, D. Clement, Y. Levron, M. Rodriguez, and D. Maksimovic, "Performance of power-limited differential power processing architectures in mismatched PV systems," *IEEE Trans. Power Electron.*, vol. 30, no. 2, pp. 618–631, Feb. 2015.
[37] L. F. Lavado Villa, T. Ho, J. Crebier, and B. Raison, "A power electronics equalizer application for partially shaded photovoltaic modules," *IEEE Trans. Ind. Electron.*, vol. 60, no. 3, pp. 1179–1190, Mar. 2013.

Jiahui Jiang (Member, IEEE) was born in Zhangzhou, China, in 1989. He received the B.S. and Ph.D. degrees in electrical engineering from Fuzhou University, Fuzhou, China, in 2012 and 2018, respectively.

He is currently a Lecturer with the College of Electrical Engineering, Qingdao University, Qingdao, China. His current research interests include power electronics conversion, renewable energy source generating and digital control.

Tao Zhang was born in Shandong, China, in 1997. He received the B.S. degree in electrical engineering in 2019 from Qingdao University, Qingdao, China, where he is currently working toward the M.S. degree in power electronics and drives.

He is currently studying and analyzing renewable energy applications and bidirectional ac–dc converters.

Daolian Chen (Senior Member, IEEE) was born in Fujian, China, in 1964. He received the B.S., M.S., and Ph.D. degrees and the Postdoctoral Certification from the Department of Electrical Engineering, Nanjing University of Aeronautics and Astronautics (NUAA), Nanjing, China, in 1986, 1989, and 1998, and 2001, respectively.

He was a Teaching Assistant, a Lecturer, an Associate Professor, and a Professor with the Department of Electrical Engineering, NUAA, in 1989, 1991, 1996, and 2002, respectively. He was a Professor with the College of Electrical Engineering, Fuzhou University, Fuzhou, China, in 2005. He has been the Chief Professor of the College of Electrical Engineering, Qingdao University, Qingdao, China, since 2017. He has been a Delta Scholar, and the National Outstanding Professional and Technical Personnel, since 2014, and the Millions of Leading Engineering Talents in the National Ten Thousand Talent Program, China, since 2016. He has been the Dean of the College of Electrical Engineering, Qingdao University, since 2018. He has authored or coauthored three works and more than 100 technical articles. He is the holder of 21 invention patents. His research interests include power electronics conversion, new energy source generating, and aviation electrical power supply systems.

Dr. Chen was the recipient of one National and three Province Class Reward Productions of Science and Technology.